CHEMISTRY OF MATERIALS

pubs.acs.org/cm

Article

Chloride Insertion Enhances the Electrochemical Oxidation of Iron Hydroxide Double-Layer Hydroxide into Oxyhydroxide in Alkaline Iron Batteries

Sathya Narayanan Jagadeesan, Gabriel D. Barbosa, Fenghua Guo, Lihua Zhang, A. M. Milinda Abeykoon, Gihan Kwon, Daniel Olds, C. Heath Turner, and Xiaowei Teng*

Cite This: *Chem. Mater.* 2023, 35, 6517−6526

Read Online

ACCESS | Metrics & More | Article Recommendations | Supporting Information

ABSTRACT: Rechargeable alkaline iron batteries that constitute environmentally benign electrolytes and earth-abundant industrial materials are desirable green solutions for large-scale energy storage. As one of the most abundant metal elements in the earth's crust, iron (Fe) can satisfy nearly all criteria for low-cost and safe battery electrodes. However, challenges in achieving reversible Fe redox impede their extensive implementation in modern energy supply systems. This study revealed that Cl-anion insertion into $Fe(OH)_2$ layered double hydroxide (LDH) formed a green rust intermediate phase with the formula $[Fe_2^{2+}Fe_1^{3+}(HO^-)_6]^+[Cl]^-$, which assisted a high $Fe(OH)_2$/FeOOH conversion reaction (64.7%) and improved cycling stability. This new iron redox chemistry was validated by *operando* X-ray diffraction, electrochemical testing, X-ray absorption spectroscopy (XAS), X-ray photoelectron spectroscopy (XPS) analysis, scanning transmission electron microscopy−energy-dispersive X-ray spectroscopy (STEM-EDS) mapping, and molecular dynamics (MD) simulations. Our study provides new insight into designing LDH materials for high-capacity alkaline iron batteries.

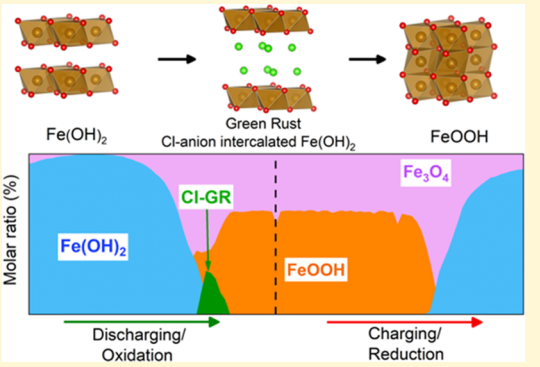

INTRODUCTION

Stationary battery systems are pivotal to implementing renewable energy for a net-zero world by storing electricity from solar panels or wind turbines during peak production to accommodate fluctuating demand at the macro level.[1] Lithium-ion batteries (LIBs) based on intercalation chemistry have been widely used. However, high cost and safety concerns from the flammable organic electrolytes and limited reserves of critical materials such as lithium and cobalt impede their large-scale implementations in stationary storage.[2] Rechargeable aqueous batteries that constitute environmentally benign electrolytes and earth-abundant materials such as iron, aluminum, and magnesium become desirable by offering green and safe battery chemistry.[3,4]

Among various aqueous rechargeable batteries, Ni−Fe and Fe−air batteries using earth-abundant and low-cost constituent elements have theoretical energy densities of 476 and 1431 Wh/kg, respectively.[5−7] Significant achievements have been made in developing Ni oxides and hydroxides cathode materials for Ni−Fe alkaline batteries with improved storage capacity and cycling life, as well as earth-abundant transition-metal oxide electrocatalysts as the oxygen electrode (cathode) for Fe−air batteries with decreased overpotential for oxygen reduction reaction and oxygen evolution reaction.[8,9] However, the poor performance of Fe-based anodes has been the main obstacle to the further implementation of Ni−Fe and Fe−air alkaline batteries for modern stationary energy storage. The main technical challenge for the anode redox is the poor coulombic efficiency, rooted in the formation of H_2 on the charge cycle and poorly conductive Fe_3O_4 on the discharge cycle. Considerable research efforts have been spent to address the limitations of Fe redox. It is found that depositing catalytically inactive FeS or Bi/Pb materials on the Fe anode augments HER overpotential during the charging process.[10,11] Thus, during the deep charge process, hydrogen production can be partially suppressed, and the coulombic efficiency of the Fe anode reactions is improved. On the other hand, several approaches are reported to mitigate the conductivity loss upon forming the Fe_3O_4 discharge product, including the nano-structured electrode design to enhance the contact between electrode materials and electrolytes or introducing high-surface and high-conductivity carbon nanotubes or reduced graphene oxides to enhance electrical conductivity.[8] These approaches improve the Fe redox in alkaline media. However, they do not

Received: June 15, 2023
Revised: July 20, 2023
Published: August 2, 2023

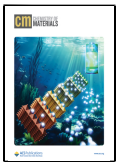

fundamentally suppress the formation of H_2 or Fe_3O_4, and thus, the coulombic efficiencies in most reported studies remain low (<60%).

Although anion intercalation into graphite was first reported in 1938,[12] anion storage batteries have not been intensively studied. Most battery systems relying on an intercalation charge storage mechanism utilize metal oxides with a negatively charged metal-oxygen molecular framework allowing the insertion of positively charged cations (e.g., Li, Na) into the spacing between metal-oxygen layers. Anion storage has been reported in several redox-active polymers such as polypyrrole and polythiophene analogues,[13−16] but anion storage in metal oxides has only found limited success. Layered double hydroxides (LDHs) are an interesting group of layered metal hydroxides with a uniquely positively charged metal-oxygen molecular framework with a formula of $[M_{1-x}^{2+}N_x^{3+}(HO^-)_2]^{x+}[(X^{n-})_{x/n}]^{x-}$, where M and N could be the same transition-metal cation, and X is the intercalated anion. Therefore, LDHs show promising separation, catalysis, and energy storage applications since the interlayer structures can be tuned to intercalate different anions selectively.[17−21] However, realizing electrochemical intercalation of Cl^- in LDH electrode materials is still in its infancy. Several studies have studied the structure−property relationships involved during the Cl^- transport in LDHs,[22,23] though explicit structural evidence from *in situ* and *operando* studies is still lacking. Recently, it was reported that the insertion of SO_4^{2-} anions into $Fe(OH)_2$, a brucite-type layered double hydroxide (LDH), assisted the conversion of $Fe(OH)_2$ into FeOOH during the electro-oxidation process in an alkaline solution.[24] Anion-intercalated $Fe(OH)_2$ is called green rust (GR), having a chemical formula of $[Fe_{1-x}^{2+}Fe_x^{3+}(HO^-)_2]^{x+}(A_{x/n}^{n-})^{x-}$, where anions ($A^{n-}$) are intercalated between the Fe−O interlayers. In the iron−water Pourbaix diagram, the GR phase connects $Fe(OH)_2$ and FeOOH in mildly alkaline solutions. Thus, $Fe(OH)_2 \rightarrow GR \rightarrow FeOOH$ redox becomes viable to realize $Fe(OH)_2$/FeOOH conversion in the presence of anion intercalation. While the reported FeOOH formation assisted by SO_4^{2-}insertion paves a new pathway toward efficient utilization of Fe redox for Fe alkaline batteries such as Fe−air battery or Fe−Ni battery, only 20% $Fe(OH)_2$ was converted into FeOOH upon discharging, and Fe_3O_4 remained the major discharge product. This might be attributed to the sluggish transport kinetics of SO_4^{2-} and its strong electrostatic interaction with the Fe−O molecular layer due to its bivalent nature.

Notably, Cl^- ions could be a better intercalating agent for reversible insertion and extraction than SO_4^{2-} during the GR formation for the following reasons. First, Cl^- has a spherical geometry, while SO_4^{2-} has a tetrahedral molecular geometry. Thus, Cl^- has a smaller ionic radius (1.81 Å versus 2.90 Å) or a hydrated ionic radius (3.32 Å versus 3.70 Å) than SO_4^{2-}, and Cl^- transport in interlayers of LDHs has a lower percolation barrier. Second, the monovalent nature of Cl^- causes less drastic distortion of the Fe−O molecular framework due to their modulated electrostatic interaction, in stark contrast to the strong interaction between divalent SO_4^{2-} and positively charged Fe−O molecular framework. Therefore, the enhanced Cl^- ion transport will promote the formation of Cl-LDH via a Cl^- insertion process and the conversion from $Fe(OH)_2$ to FeOOH. However, electrochemical storage of Cl anion has been reported in limited cases. $FeCl_3$ and $CoCl_2$ can act as cathode materials for Cl^- storage, while Lewis acid/base reaction with Cl^- in the aqueous electrolyte leads to the formation of soluble $FeCl_4^-$ and $CoCl_4^-$ complex.[25,26] Metal oxychlorides such as VOCl and FeOCl can store Cl^- but only in a nonaqueous electrolyte (propylene carbonate) using an organic chloride salt.[26] BiOCl can achieve Cl^- storage only in an acidic aqueous electrolyte, while most of the Fe batteries appear to be more operative in an alkaline solution to avoid the formation of dissoluble Fe species.[27,28]

In this study, we show strong structural evidence, for the first time, to demonstrate that Cl-anion insertion can be achieved in $Fe(OH)_2$ LDH host materials in a mildly alkaline solution. The *operando* XRD tests suggested that although Cl-anion insertion into $Fe(OH)_2$ only occurred in a limited voltage window, the resulting Cl-intercalated GR phase (Cl-GR) intermediate phase significantly improved $Fe(OH)_2$/FeOOH conversion (64.7%) and cycling stability. Reversible $Fe(OH)_2$ to FeOOH redox in the presence of GR phase formation chemistry shows a high discharge capacity of 165 mAh/g in half-cell and excellent average coulombic efficiency of ∼90% after 400 charge−discharge cycles in full-cell tests. Furthermore, molecular simulations corroborate the strong interactions between Cl^- anions and the LDH surfaces even without electrode charge.

EXPERIMENTAL SECTION

Material Synthesis and Characterizations. The following chemicals were used for synthesis as purchased: 2.085 g of ferrous sulfate heptahydrate ($FeSO_4{\cdot}7H_2O$) (Alfa Aesar) was mixed with 0.66 g of ferric sulfate ($Fe_2(SO_4)_3{\cdot}xH_2O$) (Sigma-Aldrich) and dissolved in 50 mL of degassed deionized (DI) water. The solution was stirred at 350 rpm for 15 min, while 50 mL of a 0.3 M NaOH (Alfa Aesar) solution was added to the colloidal mixture. The solution was stirred at 850 rpm under the argon overhead for 24 h. Then, the product was centrifuged and washed with degassed DI water three times before drying under argon gas overnight. Thus, synthesized green-colored iron oxide was finely grounded and stored under an inert gas-filled desiccator. To find the amount of water associated with the material, the sample was annealed from room temperature to 150 °C for 30 min for 1 h and cooled back to the initial temperature. The difference in mass before and after baking was related to the water loss, which was calculated to be 15%. The mass calculations conducted in all of the experiments were calibrated according to this value.

Scanning Electron Microscopy (SEM). SEM images were captured from Tescan Lyra3 GMU FIB-SEM at the University Instrumentation Center (UIC), University of New Hampshire. The carbon-painted stub was used as the substrate, and the powdered sample was sputtered on top with 12 nm of Au−Pd alloy.

X-ray Photoelectron Spectroscopy (XPS). XPS was carried out in Kratos Axis Supra XPS at the UIC using the Mg Kα monochromator. The XPS samples were the 6 mg of 7:3 ratio of active material and carbon black loaded on the carbon papers and collected after conducting three-electrode CP measurements. These electrodes were stopped at different potentials during CP and studied in ultrahigh vacuum of $\sim 10^{-8}$ Torr. CasaXPS software was used to process and analyze the obtained results, and all of the spectra were calibrated according to the adventitious carbon (C 1s) peak at the binding energy of 284.8 eV.

Synchrotron X-ray Scattering. The *operando* synchrotron X-ray diffraction (XRD) studies were conducted at the beamline 28-ID-1 of Brookhaven National Laboratory with a wavelength of 0.1665 Å. The active material was coated on 5% Toray carbon papers with a ratio similar to the half-cell studies and assembled into a homemade three-electrode cell. The XRD images were collected on a 2D array detector simultaneously, while the sample performed cyclic voltammetry (CV). All of the acquired patterns were phase analyzed by the Rietveld refinement method in the GSAS-II software. The synchrotron instrument parameters were calibrated by the CeO_2 standard. The

https://doi.org/10.1021/acs.chemmater.3c01496
Chem. Mater. 2023, 35, 6517−6526

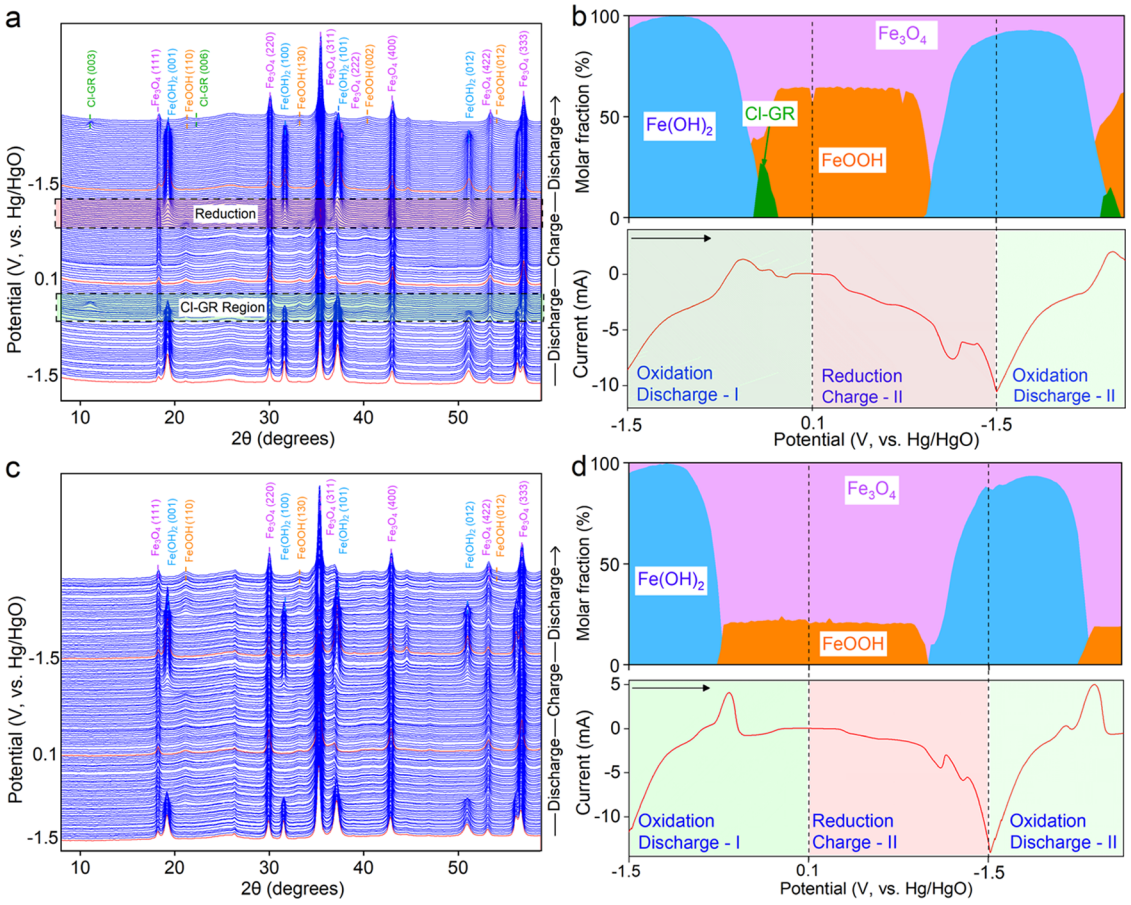

Figure 1. (a, c) Complete waterfall plots and (b, d) phase ratio analyses of iron oxides in (a, b) NaOH/NaCl and (c, d) NaOH electrolytes using *operando* XRD measurements along with cyclic voltammetry at the scan rate of 0.5 mV/s. The selected regions in (a) show the phase transitions during the Cl^- insertion (discharge) and $Fe(OH)_2$ formation (charge). They highlight the XRD patterns depicting the Cl-GR formation when iron oxides were discharged from −0.42 to −0.18 V and the $Fe(OH)_2$ formation when iron oxides were charged from −1.02 to −1.5 V, respectively. The X-ray wavelength is corrected to Cu Kα source (λ = 1.5406 Å). Arrows in (b) and (d) point to the voltage scan direction.

patterns were re-plotted with respect to the Cu Kα radiation wavelength (λ = 1.5406 Å) in this manuscript. Notably, *operando* XRD only reveals the long-range order structural details of the materials by analyzing the Bragg diffraction pattern under the assumption that the local structure of the materials (e.g., disorder, amorphization, site defect) was assumed unchanged. In addition, the grain size of the materials was also assumed constant since the sizes of the particles are relatively large (~100 nm).

High-Resolution Transmission Electron Microscopy (HR-TEM). HR-TEM was conducted at the Electron Microscopy Facility at the Center for Functional Nanomaterials in Brookhaven National Laboratory. The instrument used for high-angle annular dark-field (HAADF) imaging was an FEI Talos F200x scanning/transmission electron microscope equipped with an X-FEG electron source module and operated at 200 keV. The elemental mapping of the discharge sample was done by a four-quadrant 0.9-sr energy-dispersive X-ray spectrometer (EDS).

X-ray Absorption Spectroscopy (XAS). XAS measurements were done at beamline 6-BM Beamline for Materials Measurement at the National Synchrotron Light Source II, Brookhaven National Laboratory. The samples were prepared by drop-casting 2 mg of active material with the same ratio as used for half-cell measurements. The samples were cycled with CV in corresponding electrolytes and held at the oxidation potential of 0.2 V (versus Hg/HgO) for 15 min and dried under vacuum before placing them for data collection. The XAS measurements were carried out in transmission mode at the Fe K-edge (7112 eV). Fe metal foil and iron oxide powders (Fe_3O_4 and FeOOH) were references for X-ray energy calibration and data alignment. Athena software from the Demeter package was used for XAS data processing and analysis.

Electrochemical Measurements. Half-cell chronopotentiometry (CP) measurements were conducted in CH Instruments 660D/E electrochemical potentiostat. Three-electrode cell was assembled using the glassy carbon (Pine Research Instrumentation) drop-coated with active material as the working electrode, platinum wire as the counter, and mercury/mercury oxide reference electrode (Pine Research Instrumentation). The coating ink was prepared using the 7:3 ratio of active material to carbon black mixture in deionized (DI) water. 40 μg of active material and 20 μL of 1% Nafion 117 (Sigma-Aldrich) were loaded on the working electrode. The electrolyte consisted of sodium hydroxide (NaOH) (Alfa Aesar), sodium chloride (NaCl) (Alfa Aesar), and small amounts of sodium silicate (Na_2SiO_3) (Sigma-Aldrich). All of the electrolytes were degassed using flowing argon gas for at least 2 h before every measurement.

Long-term cycling was conducted by assembling asymmetric two-electrode full cell in ECC-Aqu electrochemical cells (EL-Cell) using the active material as the negative electrode and overloaded active carbon as the positive electrode. The anode ink was prepared by mixing 20% sample, 80% carbon black, and 8.68 μL of styrene-butadiene rubber (SBR, MTI) in 0.8 mL of ethanol and 0.2 mL of DI H_2O. While cathode ink consists of 200 mg Vulcan XC-72R (Fuel cell store), and 86.84 μL SBR mixed in 16 mL of ethanol. Toray carbon papers with 40% Teflon (Fuel cell earth) were cut into 18 mm disks and drop-coated with the respective inks. Five pieces of Whatman filter papers (11 μm pore size) were used as the separator and soaked with 3 mL of the electrolyte solution. The full-cell CP measurements

https://doi.org/10.1021/acs.chemmater.3c01496
Chem. Mater. 2023, 35, 6517−6526

were performed at 0.2 A/g using the Arbin BT-G battery cycler (S/N: 177 907).

Molecular Dynamics Simulations. The molecular dynamics simulations were performed using Gromacs 2021.1.[29] CLAYFF was used to model Fe_2O_3 interactions,[30] and the SPC/E water model was used to model bonded and nonbonded water interactions.[31] Consistent with the CLAYFF force field, the interactions between unlike atom pairs were calculated using Lorentz-Betherlot mixing rules. The NaCl was modeled using Joung and Cheatham force field,[32] and a cutoff radius of 1.2 nm was used for coulombic and Lennard-Jones interactions. Based on the crystallographic structure of Fe_2O_3,[33] the initial box configurations were built using the Packmol package.[34] In our approach, the effect of confinement was explicitly evaluated by looking at two different scenarios, in which the first was built using 100 molecules of NaCl and 5000 molecules of water, and the last one using 100 molecules of NaCl and 10 000 molecules of water so that an aqueous bulk phase would be recovered. Each system was run in triplicate to diminish the influence of the initial conditions and minimize kinetic effects.

The energy of the initial configurations was minimized using the steepest descent algorithm, followed by an initial equilibration stage of 400 ns. Then, production simulations were run for a total of 100 ns, during which data was collected. To achieve a smooth density during the equilibration stage, the semi-isotropic Berendsen barostat[35] with a time constant of 2 ps was used during the first 50 ns; after this, the semi-isotropic Parrinello-Rahman barostat was used,[36,37] with time constants of 5 ps; the v-rescale thermostat was employed,[38] in order to maintain the constant temperature condition at 298 K, with a time constants of 0.1 ps. Finally, the long-range corrections to the coulombic interactions were calculated using the particle mesh Ewald (PME).[39]

RESULTS AND DISCUSSION

The iron oxide materials were synthesized by co-precipitating ferric and ferrous salts in an alkaline solution (See material synthesis in the Supporting Information). Figure S1 shows the scanning electron microscope (SEM) image of the as-synthesized iron (II, III) oxides, revealing a morphology of nanoparticles (average diameter of ∼50 nm) and short nanorods (average width of ∼40 nm and length of ∼150 nm). The transmission electron microscope (TEM) images (Figure S2) corroborated with SEM. The Rietveld refinement of synchrotron XRD suggested the as-synthesized materials consisted of 75.5% (molar ratio based on the total Fe atoms) of goethite (α-FeOOH) and 24.5% of magnetite (Fe_3O_4), as shown in Figure S3. The Bragg diffraction peaks at 2θ angles of 33.17, 36.59, and 53.1°, indexing to (130), (111), and (221) planes of α-FeOOH (JCPDS: 00-100-8767), respectively. The remaining diffraction peaks, such as (311), (400), and (440), at 2θ = 35.5, 43.19, and 62.66°, were attributed to Fe_3O_4 (JCPDS: 00-900-2673).

Figure 1 shows *operando* XRD measurements of iron oxides, acquired simultaneously along with cyclic voltammetry (CV) electrochemical measurements, conducted between −1.5 and 0.1 V (versus Hg/HgO) at a voltage scan rate of 0.5 mV/s, in two different electrolytes, 0.1 M NaOH and 0.1 M NaOH/0.45 M NaCl. A trace amount of Na_2SiO_3 additive (1000 ppm) was added to the electrolyte to improve the chemical stability of Fe-based electrodes.[40] The potentiodynamic evolution of the crystalline structure of iron oxides during cycling was studied from the Rietveld refinement of diffraction patterns to understand the charge storage processes related to various iron oxide/hydroxide conversion reactions. Figure 1a,c shows the waterfall patterns of the XRD data obtained from NaOH/NaCl and NaOH electrolytes, respectively. Figure 1b,d reveals the corresponding molar ratio analysis from the Rietveld refinements.

Figure 1a,b shows the *operando* XRD analysis of iron oxides in NaOH/NaCl. Iron oxides, a mixture of α-FeOOH and Fe_3O_4 at pristine state, were nearly completely reduced to $Fe(OH)_2$ (JCPDS 13-0089) at −1.5 V, evidenced by characteristic (001), (100), and (012) diffraction peaks at 2θ angles of 19.2, 31.6, 51.0°. When $Fe(OH)_2$ was discharged (oxidized) from −1.5 V to higher voltage values of −0.89 and −0.59 V, Fe_3O_4 and FeOOH formed, as shown in eqs 1 and 2, with signature Fe_3O_4 peaks of (111), (220), (311), and (222) and signature FeOOH peaks of (110), (130), and (021). When potential further increased to −0.43 V, a new set of diffraction peaks emerged at 2θ angles of 11.2, 22.3, and 32.4°, indexed to the (003), (006), and (101) reflections of the Cl-intercalated green rust (Cl-GR, JCPDS 04-0127). Notably, the Cl-GR phase with a formula of $[Fe_2^{2+}Fe_1^{3+}(HO^-)_6]^+[Cl]^-$ results from the Cl^- intercalation in between the Fe−O molecular layers of $Fe(OH)_2$. The insertion of Cl^- accompanies with partial oxidation of Fe^{2+} into Fe^{3+}. At the same time, Fe−O molecular frameworks uphold a stable layered structure (eq 3). More importantly, the Rietveld refinement shows that the FeOOH molar ratio drastically increased from 34.9 to 64.0% after the formation of Cl-GR, suggesting Cl-GR significantly improved the FeOOH formation conversion (eq 4). Once the Cl-GR phase completely diminished when the potential increased to −0.22 V, the FeOOH molar ratio (based on total Fe atoms) reached its maximum value (64.7%) and remained at this value even though the potential continuously increased to the fully discharged state at 0.1 V. This dynamic phase evolution suggests Cl-GR is an active intermediate phase, facilitating the Fe^{2+}/Fe^{3+} conversion via a $Fe(OH)_2$ → Cl-GR → FeOOH pathway and avoiding the $Fe(OH)_2$ → Fe_3O_4 pathway. During the consecutive charging process from 0.1 to −1.5 V (reduction), the $Fe(OH)_2$ and Fe_3O_4 formed nearly simultaneously when the charging potential reached −0.83 V. Continuously charged to −1.5 V, all of the Fe_3O_4 materials were reduced to $Fe(OH)_2$.

$$3Fe(OH)_2 + 2OH^- \rightarrow Fe_3O_4 + 4H_2O + 2e^- \quad (1)$$

$$Fe(OH)_2 + OH^- \rightarrow FeOOH + H_2O + e^- \quad (2)$$

$$3Fe(OH)_2 + Cl^- \rightarrow [Fe^{2+}{}_2Fe^{3+}{}_1(HO^-)_6]^+[Cl]^- + e^- \quad (3)$$

$$[Fe^{2+}{}_2Fe^{3+}{}_1(HO^-)_6]^+[Cl]^- + 3OH^- \rightarrow 3FeOOH + Cl^- + 3H_2O + 3e^- \quad (4)$$

Notably, the Cl-GR-assisted $Fe(OH)_2$/FeOOH conversion is repeated in the consequential cycles (Region Discharge II in Figure 1b), suggesting a highly reversible nature. It is to be noted that the GR phase only occurs on discharge, and the charging process proceeds from FeOOH → $Fe(OH)_2$ and Fe_3O_4 → $Fe(OH)_2$ without forming a GR intermediate, even though GR is a thermodynamically viable phase between $Fe(OH)_2$ and FeOOH. This observation implies that the FeOOH → GR charging process is kinetically slower than GR → Fe_3O_4 → $Fe(OH)_2$, while $Fe(OH)_2$→GR discharging process is kinetically faster than GR → Fe_3O_4 or GR → FeOOH. Thus, the accumulation of the GR phase is only observed from XRD in the discharging process. The high-

https://doi.org/10.1021/acs.chemmater.3c01496
Chem. Mater. 2023, 35, 6517−6526

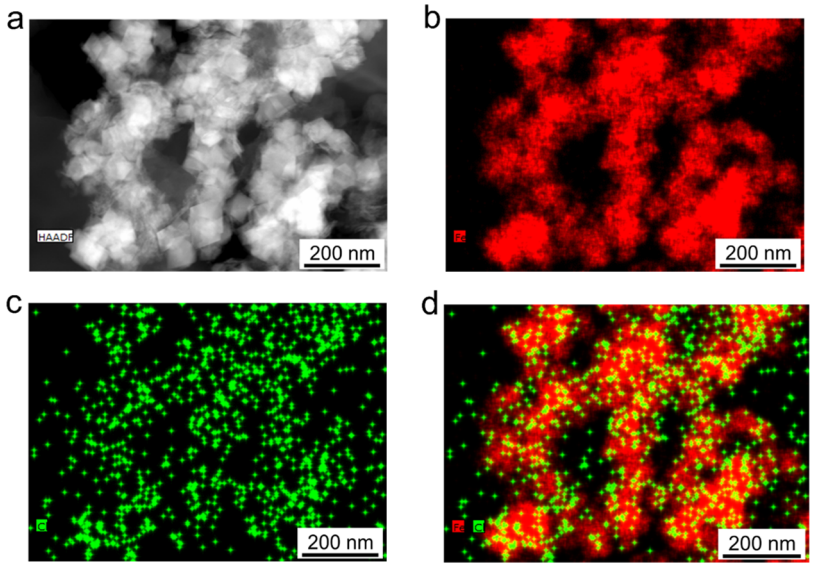

Figure 2. (a) HAADF image of iron oxides discharged at −0.66 V in NaOH/NaCl electrolyte. The elemental mapping by STEM-EDS shows the distributions of (b) Fe (red), (c) Cl (green), and (d) combined Fe and Cl.

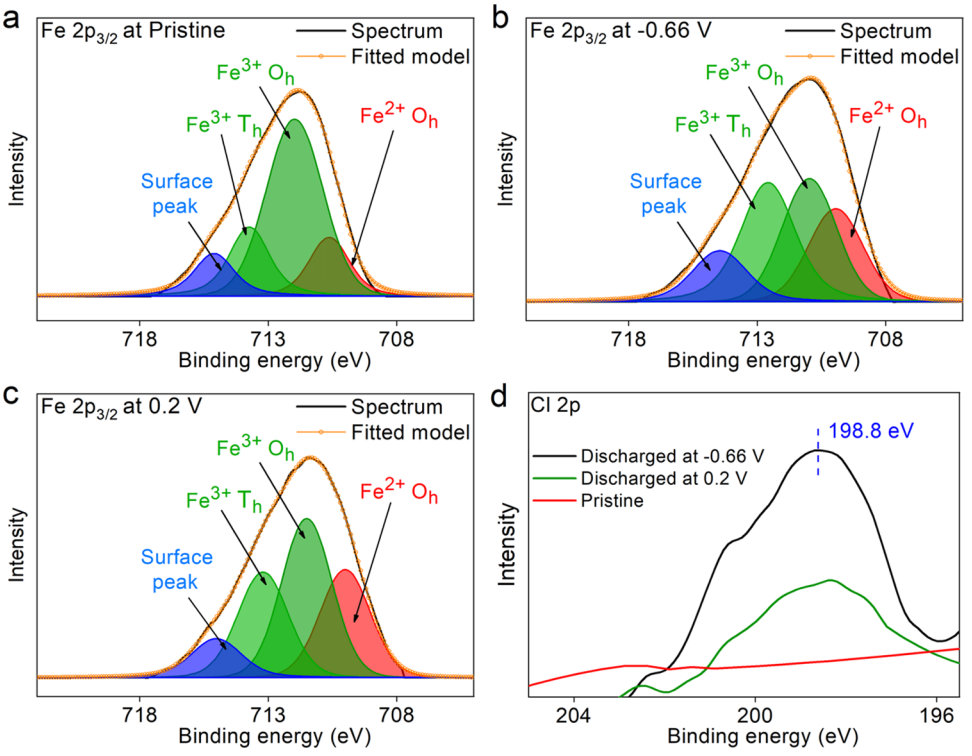

Figure 3. XPS analysis of multiplet splitting of Fe $2p_{3/2}$ at the (a) pristine state and after discharging at (b) −0.66 V and (c) 0.2 V. (d) Cl 2p of the iron oxides at the pristine state and after discharging at −0.66 and 0.2 V.

lighted regions of Cl intercalation and reduction of iron oxides in Figure 1c are elucidated in Figure S4. Figure 1c,d shows the *operando* XRD analysis of iron oxides in the NaOH electrolyte. Different from XRD obtained from NaOH/NaCl electrolyte, there was no GR phase observed in NaOH throughout the potential window between −1.5 and 0.1 V. Notably, the maximum molar ratio of $Fe(OH)_2$ did not appear at the most cathodic electrochemical conditions (−1.5 V in Figure 1c). Instead, it reached a maximum value when the voltage ramped from −1.5 to ca. −1.2 V. This "lagging effect", where the crystalline phase ratio shows a delayed response compared to electrochemical voltage input, is also observed in other charge and discharge segments during XRD measurements, as well as in the cell where NaOH solution was used (Figure 1d). This "lagging effort" could be explained by a fundamental timescale difference between charge transfer and lattice transformation in an off-equilibrium electrochemical condition. In addition, the time required by the X-ray data requisition could also be attributed to this lagging effect but to a minor extent.

Figure S5 shows the schematics of the homemade three-electrode electrochemical cell design used for the *operando* synchrotron measurements, as well as the comparison of CV

https://doi.org/10.1021/acs.chemmater.3c01496
Chem. Mater. 2023, 35, 6517−6526

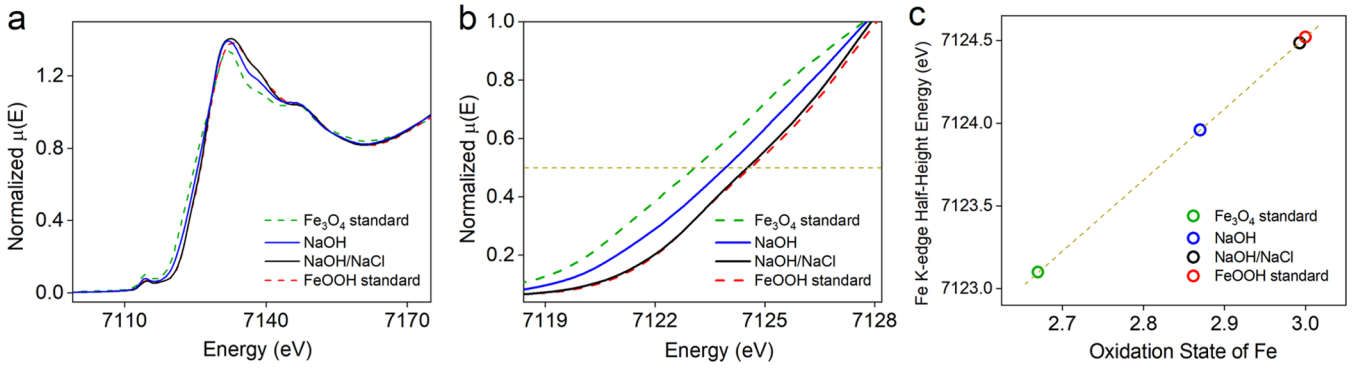

Figure 4. (a) XANES results of Fe K-edge in iron oxide sample at a fully discharged state of 0.2 V in NaOH and NaOH/NaCl electrolytes along with iron oxide standards. (b) Enlarged spectra highlighting the absorption energy shift at the half-edge step. (c) Formal oxidation states of Fe in iron oxides, determined by a linear fit of half-edge energies.

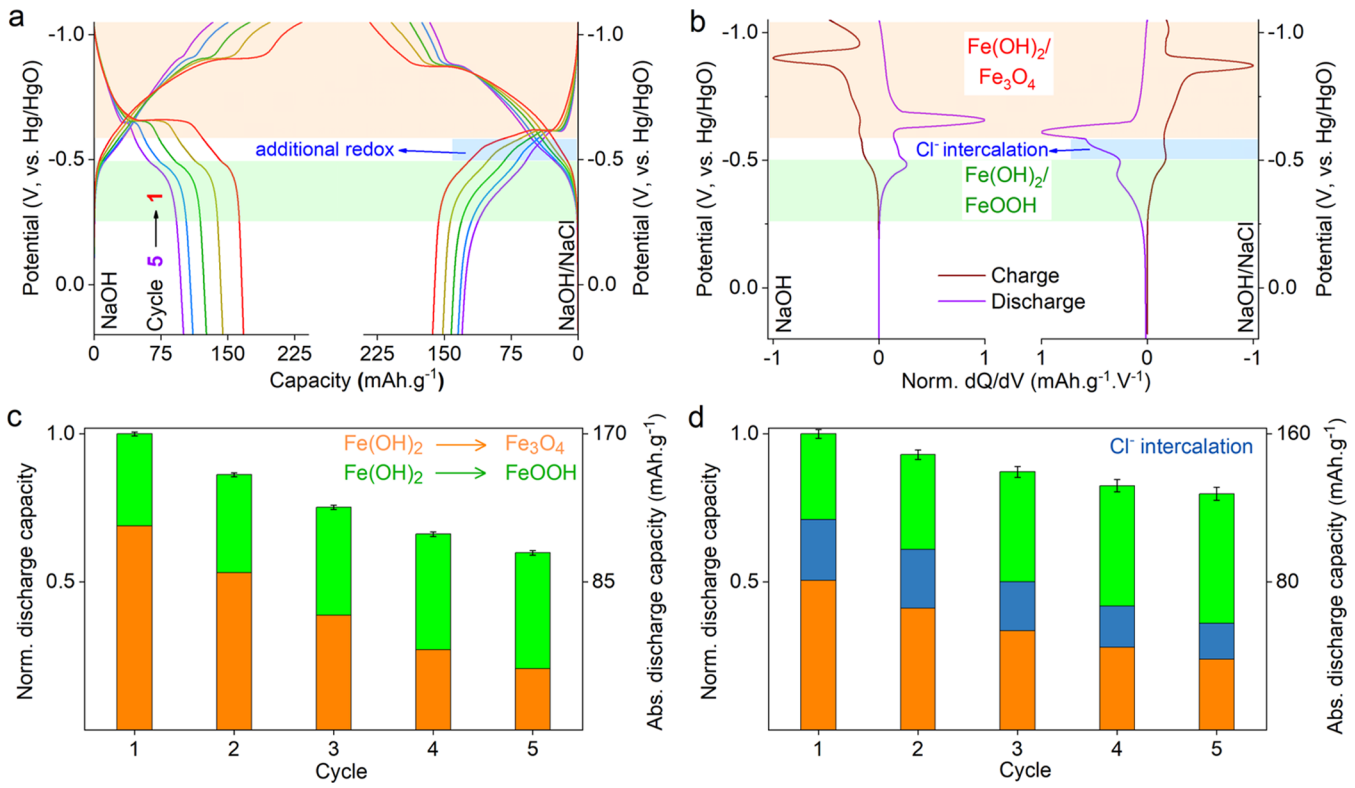

Figure 5. Half-cell cycling measurements. (a) CP curves, (b) dQ/dV plots, and the capacity ratios of each conversion redox reaction in (c) NaOH and (d) NaOH/NaCl electrolytes.

plots obtained from the *operando* electrochemical cell and three-electrode half-cell measurements. Although the *operando* cells use a much higher loading of iron oxide materials (~10 mg of ink materials with 70% iron oxide and 30% active carbon loaded on the carbon paper) than the standard lab-scale experiments (~40 μg of ink materials with 70% iron oxide and 30% active carbon loaded on the glassy carbon electrode), two measurements deliver comparable discharge capacity (108 mAh/g versus 137 mAh/g).

The intercalation of Cl ion into $Fe(OH)_2$ is supported by scanning TEM energy-dispersive X-ray spectroscopy (STEM-EDS) mapping. Figure 2a shows the high-angle annular dark field (HAADF) of the iron oxides discharged at −0.66 V (the potential at which Cl-GR reached the highest ratio). The elemental mapping of Fe, Cl, and combined Fe and Cl was presented in Figure 2b−d to visualize the compositional homogeneities in the Cl-intercalated $Fe(OH)_2$ (Cl-GR). Although Cl is a weakly scattered element compared to Fe in EDS measurement, there is a relatively uniform distribution of Fe and Cl in a large area of assembled individual particles, demonstrated by STEM-EDS mapping from other sample areas (Figure S6). The results indicated that Cl-anion insertion occurred throughout the $Fe(OH)_2$ electrode materials, delivering optimal electrochemical performance on forming FeOOH via a one-charge transfer conversion reaction.

The $Fe(OH)_2$/FeOOH conversion assisted by forming Cl-GR is also supported by X-ray photoelectron spectroscopy (XPS) measurement. Figure 3a−c shows the multiplet splitting of Fe 2p spectra of the sample at the pristine state and discharged states of −0.66 V (the Cl-ion insertion region) and 0.2 V (the most discharged state), respectively, depicting Fe^{2+} in octahedral (O_h) sites and Fe^{3+} in O_h and tetrahedral (T_h)

https://doi.org/10.1021/acs.chemmater.3c01496
Chem. Mater. 2023, 35, 6517−6526

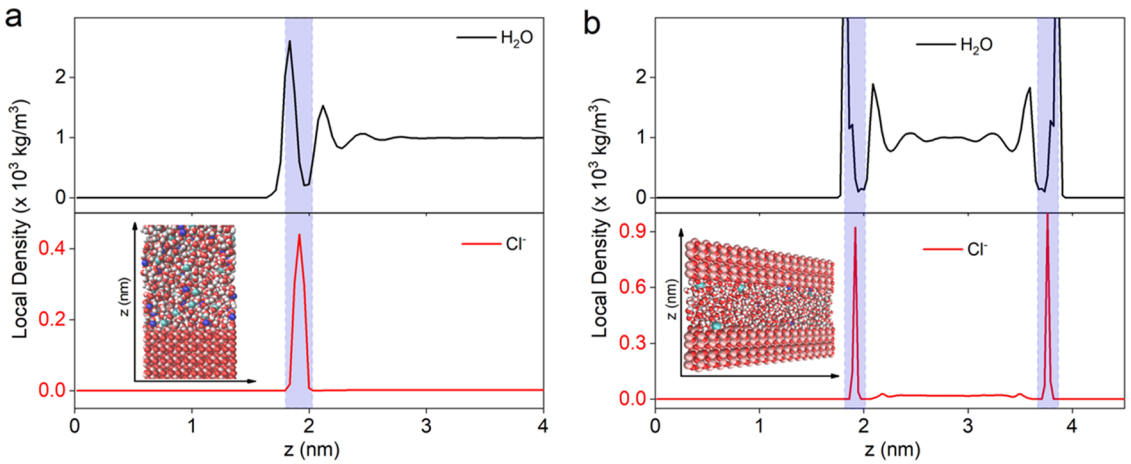

Figure 6. Density profiles of Cl^- and water perpendicular to the Fe_2O_3 surfaces in (a) wide pore (for clarity, only half of the pore is illustrated) and (b) narrow pore gaps. Illustration of the Fe_2O_3 interaction models used to evaluate relative Cl^- interactions in bulk versus confinement in (a) wide (4.68 nm) and (b) narrow pore gaps (2.13 nm) are also shown. Colors: pink = Fe, red = oxygen, white = hydrogen, blue = sodium, cyan = chloride.

sites of iron oxides. A surface peak at the binding energy of 715.1 eV also appears due to the electric charge accumulation on the substrate surface. The ratios of Fe^{3+}/Fe^{2+} are calculated to be 5.67, 2.72, and 4.56 at pristine, −0.66, and 0.2 V, respectively. They correspond to FeOOH molar ratios of 78.5, 41.8, and 71.9%, respectively, and are close to the values obtained independently from XRD refinement (75.5, 34.9, and 64.7%). Figure 3d shows the distinct Cl 2p spectra of iron oxides at the binding energy of 198.8 eV from the samples at the pristine state and discharged at −0.66 and 0.2 V. At −0.66 V, the distinct Cl signal was observed due to the high Cl-GR phase ratio at this voltage range, supporting the chloride ion intercalation obtained from XRD refinement (Figure 1) and electrochemical results from half-cell measurements (Figure 5 in a later discussion). Notably, at the fully discharged state (0.2 V), the weak but discernable Cl signal was observed from the sample. While only Fe_3O_4 and FeOOH were observed in operando XRD at 0.2 V and there was no Cl-intercalated Cl-GR phase, the observed Cl signal could be attributed to the Cl species absorbed on the electrode surface.

The Cl-GR-assisted $Fe(OH)_2$/FeOOH conversion is also supported by X-ray absorption spectroscopy (XAS) analysis. Figure 4a shows Fe K-edge XAS spectra from the fully discharged sample (0.2 V) obtained from NaOH/NaCl and NaOH electrolytes, respectively, along with Fe_3O_4 and FeOOH standards. At the fully discharged state (0.2 V), samples from NaOH/NaCl electrolyte show right-hand-shifted absorption energy at the half-edge step [1/2 μ(E)] compared to the sample made in NaOH electrolyte (Figure 4b). Figure 4c shows a linear fit of 1/2 μ(E) energy positions between $Fe^{2+/3+}$ (1/3 of Fe atoms are in 2+ and 2/3 in 3+) and Fe^{3+} spectra from Fe_3O_4 and FeOOH standards. The valences of Fe at fully discharged (0.2 V) states were quantitatively calculated to be Fe (2.87) and Fe (2.99) in NaOH and NaOH/NaCl electrolytes, respectively.

The half-cell cycling measurements provide further evidence of the high reversibility of the GR-assisted $Fe(OH)_2$/FeOOH conversion. Figure 5a shows the first five cycles of chronopotentiometry (CP) plots conducted at the current density of 0.1 A/g with potential sweeping between 0.2 and −1.05 V (versus Hg/HgO) and the corresponding first-order derivative of the discharge and charge capacity to the potential (dQ/dV), calculated from the CP curves, are shown Figure 5b (only 1st cycle dQ/dV plots are shown for clarity; more data can be found at Figure S7). Specifically, iron oxides show two similar redox features at ca. −0.65 and −0.45 V on discharging with and without NaCl additive, corresponding to $Fe(OH)_2$/Fe_3O_4 and $Fe(OH)_2$/FeOOH conversions, respectively, confirmed by *operando* XRD and Rietveld refinement. However, in the presence of NaCl, as shown in Figure 5b, iron oxides show an additional redox feature at ca. −0.58 V, which could be attributed to Cl-GR formation resulting from Cl^- intercalation into the $Fe(OH)_2$ interlayers, congruent with *operando* XRD analysis. Figure 5c,d further compares the discharge capacities contributed by $Fe(OH)_2/Fe_3O_4$, $Fe(OH)_2$/FeOOH, and Cl-GR formation processes in the first five-cycle of CP measurements. Notably, the iron oxides show similar 1st cycle discharge capacities (∼165 mAh/g) in both electrolytes with and without NaCl. However, iron oxides showed a higher discharge capacity in the 5th cycle (130 mAh/g) with the NaCl additive than without NaCl (100 mAh/g). Specifically, with Cl insertion, the discharge capacity resulting from the $Fe(OH)_2$ → FeOOH and $Fe(OH)_2$ → Fe_3O_4 pathways showed much-enhanced cycling stability than the Fe redox without NaCl additive. More repeating results of CP measurements are summarized and plotted in Figure S8. Notably, Cl-GR formation was sustained upon extended cycling. Figure S9 shows the CP and dQ/dV plots of iron oxides after 30-cycles of CP cycling, where the signature redox features at ca. −0.58 V are exclusively attributed to Cl-GR formation upon Cl^- intercalation into the $Fe(OH)_2$.

Figure 6 shows molecular dynamic (MD) simulations also corroborate the tendency for Cl-GR-assisted $Fe(OH)_2$/FeOOH conversion due to the strong tendency for Cl^- to intercalate within the LDH materials, even in the absence of electrode charge. Here, two different theoretical LDH interaction models are tested to understand the role of confinement on the NaCl solution qualitatively; one model has a large pore gap of 4.68 nm (with the center of the pore representative of the bulk NaCl aqueous solution), and the other model contains the same aqueous NaCl solution confined within a 2.13 nm wide LDH pore. For simplicity, the level of surface hydroxylation is set to zero (namely, Fe_2O_3 surface is employed), so we can isolate the effects of confinement on the Cl^- adsorption.

https://doi.org/10.1021/acs.chemmater.3c01496
Chem. Mater. 2023, 35, 6517−6526

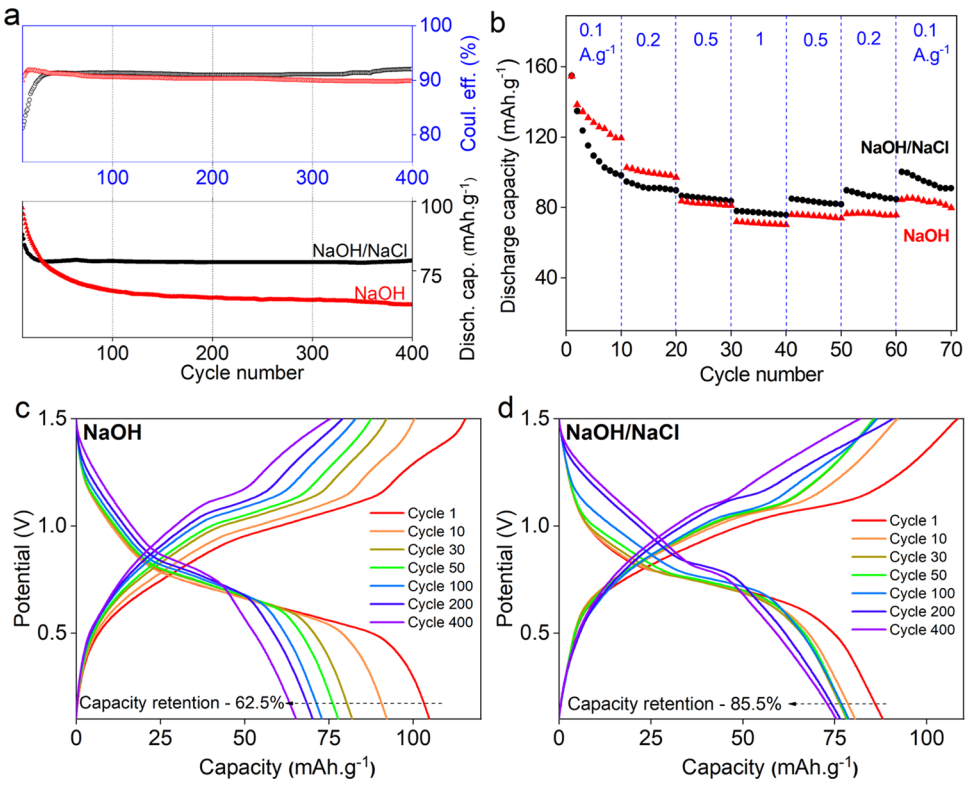

Figure 7. (a) Coulombic efficiency and discharge capacity trend and (b) rate capability tests with various current densities of iron oxides in NaOH and NaOH/NaOH electrolytes in two-electrode full cells. Charge−discharge curves in the two-electrode full cells in (c) NaOH and (d) NaOH/NaCl electrolytes at the current density of 0.2 A/g.

Figure 6a,b displays the density profile of the Cl^- anion in the 4.68 nm pore model as a function of the distance from the Fe_2O_3 surfaces. The Cl^- is strongly adsorbed to the Fe_2O_3 surface, forming a single peak at a distance slightly shifted away from the first major peak of the water density. Within the 2.13 nm pore model, the Cl^- peak becomes extremely sharp, demonstrating the significantly enhanced interactions induced by the confinement, indicating that the adsorption of Cl^- within the LDH interstitial spaces would be highly stable. While the water molecules display bulk-like behavior far from the Fe_2O_3 surfaces, the density of Cl^- is close to zero in the center region, in both the wide (Figure 6a) and narrow (Figure 6b) pore models. Although water has a strong dipole that can interact favorably with the oxide surfaces, the electrostatic interactions involving the ionic species are even stronger, leading to preferable adsorption. In addition, it has been found that the hydrogen-bond network of water is diminished within small silica pores (2.4−4.4 nm),[41] and this effect is more pronounced in the smaller pores (2.4 nm). The decrease in stability of the hydrogen-bond network within narrow pores may also be responsible for the relative enhancement of the Cl^- anions near the Fe−O surfaces within the smaller pores. Notably, the strong Cl^- anions adsorption near the Fe−O surfaces corroborates well with the *operando* XRD measurements, where a rapid formation of Cl-GR phase via the insertion of Cl^- anions into Fe−O molecular interlayers occurred at −0.43 V and thus suggested a fast Cl insertion kinetics favored by spontaneous adsorption of Cl^- anions on Fe−O surface. Moreover, *operando* XRD measurements suggested the Cl-GR diminished at a voltage of −0.22 V. This rather narrow voltage window for a stable Cl-GR phase (between −0.43 and −0.22 V) further manifest the rapid insertion and extraction kinetics of Cl^- anions, confirming their adsorption/desorption nature.

Stability of $Fe(OH)_2$/FeOOH Conversion Characterized by Electrochemical Cycling. The long-term cycling performance (400 cycles) of iron oxides was evaluated in an asymmetric two-electrode cell constructed using the iron oxide anode and an overloaded active carbon (AC) cathode, operated within a 1.5 V voltage window. The overloaded cathode had a much higher capacity than the iron oxide anode, so the overall cell capacity is close to the anode capacity, and the contribution of conducting carbon to the anode capacity has been excluded. Figure 7a shows that the iron oxides showed the capacities of 88.1 mAh/g (1st cycle) and 78.7 mAh/g (400th cycle) in the NaOH/NaCl electrolytes at a current density of 0.2 A/g, higher than those in NaOH electrolyte (62.7 mAh/g in the 400th cycle). Iron oxide/carbon full cells showed an average coulombic efficiency of 92% during the 400-cycle CP cycling, benefited by the Cl-intercalation-assisted $Fe(OH)_2$ → GR → $FeOOH/Fe_3O_4$ conversion reaction. The rate capability tests were done in current densities ranging from 0.1 to 1 $A{\cdot}g^{-1}$ to compare the performance under rigorous conditions in NaOH and NaOH/NaCl electrolytes (Figure 7b). Iron oxides in NaOH had a higher discharge capacity of 125.8 and 99.7 $mAh{\cdot}g^{-1}$ than the NaOH/NaCl electrolyte (106.2 and 91.0 $mAh{\cdot}g^{-1}$) in the initial cycles of 0.1 and 0.2 $A{\cdot}g^{-1}$. However, NaOH/NaCl electrolyte delivers a higher capacity retention than NaOH electrolyte (87.2% versus 65.3%). Moreover, the CP curves of the full cell in Figure 7c,d show better discharge capacity retention with NaCl additive (62.5% versus 85.5%). Their dQ/dV curves in Figure S10 also depict the long-term stability of the iron conversion redox, though two redox feature shifts to

https://doi.org/10.1021/acs.chemmater.3c01496
Chem. Mater. 2023, 35, 6517−6526

the higher potential across the cycles, a sign of increasing overpotential over long-term cycling. Notably, to mitigate the possible gas evolution reaction, a lower iron oxide active material loading (20%) was used in full-cell measurements than half-cells (70%) when a current density of 0.2 A/g was used, as shown in Figure 7. However, the full cells with 70% active materials loading perform well under a higher current density (1 A/g), as shown in Figure S11.

The interplay between Cl ion, $Fe(OH)_2$, and water molecules during the electrochemical cycling is complicated, and the exact mechanism of Cl ion on $Fe(OH)_2$/FeOOH conversion is still far from settled. However, our results suggest that the Cl ion might stabilize the electrode surface for better cycling stability and not necessarily improve the overall discharge capacity. This interface stabilization mechanism of Cl ion agrees with the MD simulation suggesting strong absorption of Cl ion on the Fe−O surface in the confined interlayer region and corroborates with the electrochemical measurements. The interface stabilization mechanism of NaCl additives contributed to the long-term cycling stability of the iron oxide electrode, as shown in Figure 5. Moreover, Figure S12 shows that 1st cycle discharge capacity of iron oxide in a more concentrated NaCl solution (1 M) was very close to that in 0.45 M NaCl solution (163 mAh/g versus 165 mAh/g), suggesting NaCl addition may not significantly improve the discharge capacity. However, it is noted that the addition of 0.45 M NaCl enhanced the overall ionic conductivity of 0.1 M NaOH solution (0.025 s/cm versus 0.064 s/cm), which could help iron oxide materials sustain high capacity retention upon cycling.

CONCLUSIONS

This study has demonstrated the $Fe(OH)_2$ → Cl-GR → FeOOH conversion pathway, assisted by forming the Cl-GR phase. The MD simulations suggest strong adsorption of Cl^- anion into the Fe−O surface, confirmed by *operando* XRD analysis showing a rapid formation of the Cl-GR phase through the insertion of Cl^- anion into $Fe(OH)_2$ molecular layers. Reversible iron redox favored by the Cl-GR phase shows a high $Fe(OH)_2$-to-FeOOH conversion (64.7%) and an excellent discharge capacity of 165 mAh/g in half-cell and excellent average coulombic efficiency (~90% after 400 cycles) in full-cell tests. This result will pave a new pathway to repurpose the iron rust into reversible Fe-based anode materials in alkaline batteries for grid-scale storage.

ASSOCIATED CONTENT

Supporting Information

The Supporting Information is available free of charge at https://pubs.acs.org/doi/10.1021/acs.chemmater.3c01496.

Detailed description of the material synthesis and characterizations, electrochemical measurements, synchrotron X-ray scattering and absorption, electron microscopy, experimental procedures, and MD calculations (PDF)

AUTHOR INFORMATION

Corresponding Author

Xiaowei Teng − *Department of Chemical Engineering, Worcester Polytechnic Institute, Worcester, Massachusetts 01609, United States;* orcid.org/0000-0001-9547-7175; Email: xteng@wpi.edu

Authors

Sathya Narayanan Jagadeesan − *Department of Chemical Engineering, Worcester Polytechnic Institute, Worcester, Massachusetts 01609, United States;* orcid.org/0000-0002-1034-3862

Gabriel D. Barbosa − *Department of Chemical and Biological Engineering, University of Alabama, Tuscaloosa, Alabama 35487, United States*

Fenghua Guo − *Department of Chemical Engineering, University of New Hampshire, Durham, New Hampshire 03824, United States*

Lihua Zhang − *Center for Functional Nanomaterials, Brookhaven National Laboratory, Upton, New York 11973, United States*

A. M. Milinda Abeykoon − *National Synchrotron Light Source II, Brookhaven National Laboratory, Upton, New York 11973, United States*

Gihan Kwon − *National Synchrotron Light Source II, Brookhaven National Laboratory, Upton, New York 11973, United States;* orcid.org/0000-0002-7963-2136

Daniel Olds − *National Synchrotron Light Source II, Brookhaven National Laboratory, Upton, New York 11973, United States*

C. Heath Turner − *Department of Chemical and Biological Engineering, University of Alabama, Tuscaloosa, Alabama 35487, United States;* orcid.org/0000-0002-5707-9480

Complete contact information is available at: https://pubs.acs.org/10.1021/acs.chemmater.3c01496

Author Contributions

X.T. conceived the research idea and designed the experiments. S.N.J. contributed to material synthesis and characterizations and the electrochemical experimental measurements. F.G., S.N.J., A.M.M.A., G.K., and D.O. contributed to *operando* X-ray measurements. S.N.J. contributed to the X-ray analysis. G.D.B. performed all of the atomic-scale simulations under the guidance of C.H.T. L.Z. contributed to the TEM-EDS mapping. X.T. and S.N.J. wrote the manuscript with contributions from G.D.B. and C.H.T. X.T. supervised the project. All authors discussed the results and commented on the manuscript.

Funding

This research received financial support from the National Science Foundation under Award Number 2236704 (S.N.J., X.T.). This research used the FEI Talos 200X of the Center for Functional Nanomaterials (CFN), which is a U.S. Department of Energy Office of Science User Facility, at Brookhaven National Laboratory under Contract No. DE-SC0012704. This research used 28-ID-1 and 6-BM beamlines of the National Synchrotron Light Source II, a US Department of Energy (DOE) Office of Science User Facility operated for the DOE Office of Science by Brookhaven National Laboratory under Contract No. DE-SC0012704. The authors thank Dr. Bruce Ravel for assisting with the XAS experiments at Beamline 6-BM. The XPS used is managed by the University Instrumentation Center (UIC) at the University of New Hampshire (UNH). The authors acknowledge the assistance provided by John Wilderman of the UIC.

Notes

The authors declare no competing financial interest.

REFERENCES

(1) Dunn, B.; Kamath, H.; Tarascon, J. M. Electrical Energy Storage for the Grid: A Battery of Choices. *Science* **2011**, *334*, 928−935.
(2) Mongird, K.; Viswanathan, V.; Alam, J.; Vartanian, C.; Sprenkle, V.; Baxter, R. *DOE/PA-0204: 2020 Grid Energy Storage Technology Cost and Performance Assessment* Pacific Northwest National Laboratory & Mustang Prairie Energy, US DOE: 2020.
(3) Li, W.; Dahn, J. R.; Wainwright, D. S. Rechargeable Lithium Batteries with Aqueous Electrolytes. *Science* **1994**, *264*, 1115−1118.
(4) Suo, L.; Borodin, O.; Gao, T.; Olguin, M.; Ho, J.; Fan, X.; Luo, C.; Wang, C.; Xu, K. "Water-in-salt" electrolyte enables high-voltage aqueous lithium-ion chemistries. *Science* **2015**, *350*, 938−943.
(5) Blurton, K. F.; Sammells, A. F. Metal/air batteries: Their status and potential — a review. *J. Power Sources* **1979**, *4*, 263−279.
(6) Chakkaravarthy, C.; Periasamy, P.; Jegannathan, S.; Vasu, K. I. The nickel/iron battery. *J. Power Sources* **1991**, *35*, 21−35.
(7) McKerracher, R. D.; de Leon, C. P.; Wills, R. G. A.; Shah, A. A.; Walsh, F. C. A Review of the Iron-Air Secondary Battery for Energy Storage. *ChemPlusChem* **2015**, *80*, 323.
(8) Wu, X.; Markir, A.; Xu, Y.; Zhang, C.; Leonard, D. P.; Shin, W.; Ji, X. A Rechargeable Battery with an Iron Metal Anode. *Adv. Funct. Mater.* **2019**, *29*, No. 1900911.
(9) Cheng, F.; Chen, J. Metal−air batteries: from oxygen reduction electrochemistry to cathode catalysts. *Chem. Soc. Rev.* **2012**, *41*, 2172−2192.
(10) Manohar, A. K.; Yang, C.; Narayanan, S. R. The Role of Sulfide Additives in Achieving Long Cycle Life Rechargeable Iron Electrodes in Alkaline Batteries. *J. Electrochem. Soc.* **2015**, *162*, A1864−A1872.
(11) Manohar, A. K.; Malkhandi, S.; Yang, B.; Yang, C.; Surya Prakash, G. K.; Narayanan, S. R. A High-Performance Rechargeable Iron Electrode for Large-Scale Battery-Based Energy Storage. *J. Electrochem. Soc.* **2012**, *159*, A1209.
(12) Rüdorff, W.; Hofmann, U. Graphite salts. *Z. Anorg. Allg. Chem.* **1938**, *238*, 1−50.
(13) Beck, F.; Pruss, A. Reversible Electrochemical Insertion of Anions in Poly-para-phenylene from Aqueous-electrolytes. *Electrochim. Acta* **1983**, *28*, 1847−1855.
(14) Novák, P.; Muller, K.; Santhanam, K. S. V.; Haas, O. Electrochemically active polymers for rechargeable batteries. *Chem. Rev.* **1997**, *97*, 207−281.
(15) Nyholm, L.; Nystrom, G.; Mihranyan, A.; Stromme, M. Toward Flexible Polymer and Paper-Based Energy Storage Devices. *Adv. Mater.* **2011**, *23*, 3751−3769.
(16) Zhao, X.; Zhao, Z.; Yang, M.; Xia, H.; Yu, T.; Shen, X. Developing Polymer Cathode Material for the Chloride Ion Battery. *ACS Appl. Mater. Interfaces* **2017**, *9*, 2535−2540.
(17) Fan, G. L.; Li, F.; Evans, D. G.; Duan, X. Catalytic applications of layered double hydroxides: recent advances and perspectives. *Chem. Soc. Rev.* **2014**, *43*, 7040−7066.
(18) Goh, K. H.; Lim, T. T.; Dong, Z. Application of layered double hydroxides for removal of oxyanions: A review. *Water Res.* **2008**, *42*, 1343−1368.
(19) Song, F.; Hu, X. L. Exfoliation of layered double hydroxides for enhanced oxygen evolution catalysis. *Nat. Commun.* **2014**, *5*, No. 4477.
(20) Yin, Q.; Rao, D.; Zhang, G.; Zhao, Y.; Han, J.; Lin, K.; Zheng, L.; Zhang, J.; Zhou, J.; Wei, M. CoFe-Cl Layered Double Hydroxide: A New Cathode Material for High-Performance Chloride Ion Batteries. *Adv. Funct. Mater.* **2019**, *29*, No. 1900983.
(21) Hu, J.; Tang, X.; Dai, Q.; Liu, Z.; Zhang, H.; Zheng, A.; Yuan, Z.; Li, X. Layered double hydroxide membrane with high hydroxide conductivity and ion selectivity for energy storage device. *Nat. Commun.* **2021**, *12*, No. 3409.
(22) Zhao, J.; Wu, B.; Huang, X.; Sun, Y.; Zhao, Z.; Ye, M.; Wen, X. Efficient and Durable Sodium, Chloride-doped Iron Oxide-Hydroxide Nanohybrid-Promoted Capacitive Deionization of Saline Water via Synergetic Pseudocapacitive Process. *Adv. Sci.* **2022**, *9*, No. 2201678.
(23) Young, M. J.; Kiryutina, T.; Bedford, N. M.; Woehl, T. J.; Segre, C. U. Discovery of Anion Insertion Electrochemistry in Layered Hydroxide Nanomaterials. *Sci. Rep.* **2019**, *9*, No. 2462.
(24) Guo, F.; Jagadeesan, S. N.; Pidathala, R. T.; Kim, S.; Shan, X.; Deskins, N. A.; Abeykoon, A. M. M.; Kwon, G.; Olds, D.; Narayanan, B.; Teng, X. Revitalizing Iron Redox by Anion-Insertion-Assisted Ferro- and Ferri-Hydroxides Conversion at Low Alkalinity. *J. Am. Chem. Soc.* **2022**, *144*, 11938−11942.
(25) Hsieh, Y. T.; Lai, M. C.; Huang, H. L.; Sun, I. W. Speciation of cobalt-chloride-based ionic liquids and electrodeposition of Co wires. *Electrochim. Acta* **2014**, *117*, 217−223.
(26) Zhao, X. Y.; Ren, S. H.; Bruns, M.; Fichtner, M. Chloride ion battery: A new member in the rechargeable battery family. *J. Power Sources* **2014**, *245*, 706−711.
(27) Yu, T.; Yang, R.; Zhao, X.; Shen, X. Polyaniline-Intercalated FeOCl Cathode Material for Chloride-Ion Batteries. *ChemElectroChem* **2019**, *6*, 1761−1767.
(28) Gao, P.; Reddy, M. A.; Mu, X.; Diemant, T.; Zhang, L.; Zhao-Karger, Z.; Chakravadhanula, V. S. K.; Clemens, O.; Behm, R. J.; Fichtner, M. VOCl as a Cathode for Rechargeable Chloride Ion Batteries. *Angew. Chem., Int. Ed.* **2016**, *55*, 4285−4290.
(29) Lindahl, A.; van der Spoel, H.et al. *GROMACS 2021.1 Manual*, 2021.
(30) Cygan, R. T.; Liang, J.-J.; Kalinichev, A. G. Molecular Models of Hydroxide, Oxyhydroxide, and Clay Phases and the Development of a General Force Field. *J. Phys. Chem. B* **2004**, *108*, 1255−1266.
(31) Berendsen, H. J. C.; Grigera, J. R.; Straatsma, T. P. The missing term in effective pair potentials. *J. Phys. Chem. A* **1987**, *91*, 6269−6271.
(32) Joung, I. S.; Cheatham, T. E., III Determination of Alkali and Halide Monovalent Ion Parameters for Use in Explicitly Solvated Biomolecular Simulations. *J. Phys. Chem. B* **2008**, *112*, 9020−9041.
(33) Maslen, E. N.; Streltsov, V. A.; Streltsova, N. R.; Ishizawa, N. Synchrotron X-ray study of the electron density in [alpha]-Fe_2O_3. *Acta Crystallogr., Sect. B* **1994**, *50*, 435−441.
(34) Martínez, L.; Andrade, R.; Birgin, E. G.; Martínez, J. M. PACKMOL: a package for building initial configurations for molecular dynamics simulations. *J. Comput. Chem.* **2009**, *30*, 2157−2164.
(35) Berendsen, H. J. C.; Postma, J. P. M.; van Gunsteren, W. F.; DiNola, A.; Haak, J. R. Molecular dynamics with coupling to an external bath. *J. Chem. Phys.* **1984**, *81*, 3684−3690.
(36) Nosé, S.; Klein, M. L. Constant pressure molecular dynamics for molecular systems. *Mol. Phys.* **1983**, *50*, 1055−1076.
(37) Parrinello, M.; Rahman, A. Polymorphic transitions in single crystals: A new molecular dynamics method. *J. Appl. Phys.* **1981**, *52*, 7182−7190.
(38) Bussi, G.; Donadio, D.; Parrinello, M. Canonical sampling through velocity rescaling. *J. Chem. Phys.* **2007**, *126*, No. 014101.
(39) Darden, T.; York, D.; Pedersen, L. Particle mesh Ewald: An N·log(N) method for Ewald sums in large systems. *J. Chem. Phys.* **1993**, *98*, 10089−10092.
(40) Jagadeesan, S. N.; Guo, F.; Pidathala, R. T.; Abeykoon, A. M. M.; Kwon, G.; Olds, D.; Narayanan, B.; Teng, X. Suppressing Spinel and Hydrogen Formation to Enable High Capacity and Reversible Alkaline Iron Batteries by Silicate Additives, 2023.
(41) Yamada, S. A.; Hung, S. T.; Thompson, W. H.; Fayer, M. D. Effects of pore size on water dynamics in mesoporous silica. *J. Chem. Phys.* **2020**, *152*, No. 154704.

https://doi.org/10.1021/acs.chemmater.3c01496
Chem. Mater. 2023, 35, 6517−6526